Received: 26 May 2021 | Revised: 10 November 2021 | Accepted: 10 November 2021

DOI: 10.1002/mrm.29104

TECHNICAL NOTE

Magnetic Resonance in Medicine

High-resolution microscopic diffusion anisotropy imaging in the human hippocampus at 3T

Jiyoon Yoo | **Leevi Kerkelä** | **Patrick W. Hales** | **Kiran K. Seunarine** | **Christopher A. Clark**

Developmental Imaging and Biophysics Section, UCL Great Ormond Street Institute of Child Health, London, United Kingdom

Correspondence
Jiyoon Yoo, Developmental Imaging and Biophysics Section, UCL Great Ormond Street Institute of Child Health, 30 Guilford Street, London, WC1N 1EH, United Kingdom.
Email: jiyoon.yoo.17@ucl.ac.uk

Funding information
Biotechnology and Biological Sciences Research Council with the London Interdisciplinary Doctoral Training Program and National Institute for Health Research Great Ormond Street Hospital Biomedical Research Center

Purpose: Several neurological conditions are associated with microstructural changes in the hippocampus that can be observed using DWI. Imaging studies often use protocols with whole-brain coverage, imposing limits on image resolution and worsening partial-volume effects. Also, conventional single-diffusion-encoding methods confound microscopic diffusion anisotropy with size variance of microscopic diffusion environments. This study addresses these issues by implementing a multidimensional diffusion-encoding protocol for microstructural imaging of the hippocampus at high resolution.

Methods: The hippocampus of 8 healthy volunteers was imaged at 1.5-mm isotropic resolution with a multidimensional diffusion-encoding sequence developed in house. Microscopic fractional anisotropy (μFA) and normalized size variance (C_{MD}) were estimated using *q*-space trajectory imaging, and their values were compared with DTI metrics. The overall scan time was 1 hour. The reproducibility of the protocol was confirmed with scan–rescan experiments, and a shorter protocol (14 minutes) was defined for situations with time constraints.

Results: Mean μFA (0.47) was greater than mean FA (0.20), indicating orientation dispersion in hippocampal tissue microstructure. Mean C_{MD} was 0.17. The reproducibility of *q*-space trajectory imaging metrics was comparable to DTI, and microstructural metrics in the healthy hippocampus are reported.

Conclusion: This work shows the feasibility of high-resolution microscopic anisotropy imaging in the human hippocampus at 3 T and provides reference values for microstructural metrics in a healthy hippocampus.

KEYWORDS

b-tensor encoding, diffusion, hippocampus, microscopic fractional anisotropy, *q*-space trajectory imaging, spherical tensor encoding

1 | INTRODUCTION

Because the diffusion of water in the brain is constrained by the presence of microscopic obstacles such as cell organelles, myelin, and macromolecules, DWI enables the study of neural tissue microstructure in vivo by probing the displacements of water molecules.[1,2] Diffusion tensor imaging is a widely used diffusion MRI (dMRI) approach in which the mean apparent diffusion propagator in an imaging voxel is characterized by a diffusion tensor, from which quantitative metrics such as fractional anisotropy (FA) and mean diffusivity (MD) can be derived.[3,4] Despite its utility in research and clinical settings, the diffusion tensor cannot capture non-Gaussian diffusion and confounds orientation dispersion of anisotropic neurites with isotropic diffusion. Since the inception of DTI, significant effort has been put into the development of data acquisition and analysis methods that address these limitations.[5–7]

Diffusion tensor imaging belongs to a class of single-diffusion-encoding methods, in which diffusion is measured along a single dimension corresponding to the direction of the applied diffusion-weighting gradient.[8,9] Single-diffusion-encoding acquisitions confound the orientation dispersion of anisotropic neurites with size variance of diffusion microenvironments, resulting in a lack of specificity.[10,11] In contrast to single-diffusion encoding, multidimensional diffusion encoding (MDE) renders the dMRI signal sensitive to the displacements of water molecules that occur in a plane or in a volume.[12–14] Multidimensional diffusion encoding enables the disentanglement of microscopic diffusion anisotropy from the size variance of microenvironments and can be used to measure microscopic fractional anisotropy (μFA).[10,15–18] The value of μFA is a normalized metric of the average eigenvalue variance of the microscopic diffusion tensors that is equal to conventional FA in voxels where all the microscopic compartments are aligned.[11,19] The μFA does not depend on the orientation dispersion of axons, thus providing more information on tissue microstructure.

The human hippocampus is a complex structure located in the medial temporal lobe that plays a key role in spatial and episodic memory.[20–23] It has become an important target in neuroimaging studies for its association in several neurological disorders. Microstructural changes in the hippocampus have been studied using DTI.[24] Studies have reported changes in MD and FA associated with neurological conditions such as epilepsy,[25,26] aging,[27,28] schizophrenia,[29,30] and Alzheimer's disease,[31,32] indicating that dMRI signal is sensitive to clinically relevant microstructural changes. The hippocampus is also further characterized by distinct sublayers by the *cornu ammonis* and the dentate gyrus, and there is increasing interest in imaging hippocampal substructures, where studies have suggested there are substructure-specific microstructural changes.[33,34]

Recent advances in dMRI protocol using partial brain coverage have enabled the acquisition of 1-mm isotropic resolution DTI of the hippocampus.[35] However, due to DTI's lack of specificity, there is a need to apply more advanced dMRI methods in the study of the hippocampus. In this study, an imaging protocol for characterizing microstructural properties of the human hippocampus at 3 T using optimized MDE gradient waveforms was defined. Using the partial brain coverage strategy,[35] spatial resolution of 1.5 mm isotropic was achieved, as MDE required higher diffusion weightings. The protocol was applied in healthy volunteers and used to estimated microscopic diffusion anisotropy and isotropic size variance within the hippocampus using q-space trajectory imaging (QTI).[11] Furthermore, a shorter protocol for situations with time constraints was defined, and the scan–rescan reproducibility of the protocol was assessed.

2 | METHODS

2.1 | Participants

Eight healthy adults (4 males; 4 females; age range 25–40 years) volunteered for the study (REC #2780/001). All participants underwent diffusion-weighted MRI scans. Before the scan, a health check questionnaire and metal checklist were filled out by the volunteers to make sure the volunteers were suitable for an MRI and had no health restrictions precluding the MRI scan. Signed consent was obtained from all volunteers, in which they agreed that the data could be used for research purposes.

2.2 | Image acquisition

Participants were scanned on a Siemens Magnetom Prisma 3T with maximum gradient strength of 80 mT/m, maximum slew rate of 200 T/m/s, and a 20-channel head receive coil (Siemens Healthcare, Erlangen, Germany). Two volunteers were scanned again 7 weeks after the first scan to assess the reproducibility of the protocol.

Before the diffusion-weighted sequence, a T_1-weighted MPRAGE sequence with an isotropic resolution of 1 mm^3 was acquired to locate 30 slices (no gap) parallel to the long axis of the hippocampus, to be used in the diffusion-weighted acquisition.[35]

The diffusion-weighted data were acquired using an in-house-developed EPI sequence that enables measurements with arbitrary gradient waveforms. Optimized[36] and Maxwell-compensated[37] gradient waveforms (duration

of 77 = ms, max gradient strength ~ 75 mT/m, max slew rate = 100 T/m/s) encoding linear and spherical *b*-tensors (Figure 1) were used with *b*-values 200, 750, 1000, 1250, 1500, 1750, and 2000 s/mm^2. The acquisitions with linear tensor encoding (LTE) and spherical tensor encoding (STE) were interleaved to reduce the pressure on the gradient hardware. For both *b*-tensors, 12 directions uniformly distributed on the surface of half a sphere were used for *b*-values less than 1500, and 32 directions were uniformly distributed on the surface of half a sphere for the rest. Additionally, 41 images were acquired with no diffusion weighting. Partial brain coverage aligned along the long axis of the hippocampus was chosen to increase the resolution to 1.5 × 1.5 × 1.5 mm^3. Other relevant imaging parameters were TR = 4.6 seconds, TE = 101 ms, FOV = 216 × 216 mm^2, partial Fourier = 6/8, and GRAPPA R = 2. Every acquisition was repeated twice to increase the SNR. The total scan session duration was 1 hour (Supporting Information Table S1).

A subsampled data set containing 24% of the data was defined to assess the feasibility of the protocol in clinical situations with time constraints. The subsampled data set contained *b*-values of 200, 750, 1250, 1500, 1750, and 2000 s/mm^2 with 4, 4, 4, 16, 16, and 32 directions, respectively. The directions were chosen so that the directions for shells from 200 to 1250 s/mm^2 and from 1500 to 1750 s/mm^2 are uniformly distributed around the surface of half a sphere. The acquisitions in the subsampled data set can be acquired in 14 minutes (Supporting Information Table S1).

2.3 | Image processing

Using MRtrix3, the raw data were denoised using Marchenko-Pastur random matrix denoising,[38] and Gibbs ringing artifacts were estimated and corrected for using a subvoxel-shift algorithm.[39] Susceptibility and eddy current–induced distortions were corrected using topup and eddy in FSL.[40] The hippocampus was automatically segmented using volBrain[41] on diffusion-weighted images registered with high-resolution T_1-weighted MPRAGE using the HIPS pipeline.[42] For the scan–rescan analysis, using NiftyReg,[43] the data were registered to the half-way space between the two time points using nonlinear transformation. The hippocampus was automatically segmented, and the segmentation was transformed back to original diffusion space.

2.4 | Parameter estimation

In QTI, the tissue is modeled as a distribution of microscopic diffusion tensors, and the signal is expressed as

$$S = S_0 \exp\left(-\mathbf{b}:\mathbf{D} + \frac{1}{2}(\mathbf{b}\otimes\mathbf{b}):\mathbb{C}\right), \quad (1)$$

where S_0 is the signal without diffusion weighting; $\mathbf{b}$ is the *b*-tensor; $\mathbf{D}$ is the voxel-level diffusion tensor; $\mathbb{C}$ is the covariance tensor of microscopic diffusion tensors; denotes an inner product; and $\otimes$ denotes an outer product.[11]

The values of S_0, $\mathbf{D}$, and $\mathbb{C}$ were estimated as

$$(\ln S_0, \mathbf{D}, \mathbb{C})^T = \left(X^T H X\right)^{-1} \left(X^T H\right) S \quad (2)$$

where

$$\mathbf{X} = \begin{pmatrix} 1 & -\mathbf{b}_1^T & \frac{1}{2}(\mathbf{b}_1\otimes\mathbf{b}_1)^T \\ \vdots & \vdots & \vdots \\ 1 & -\mathbf{b}_n^T & \frac{1}{2}(\mathbf{b}_n\otimes\mathbf{b}_n)^T \end{pmatrix} \quad (3)$$

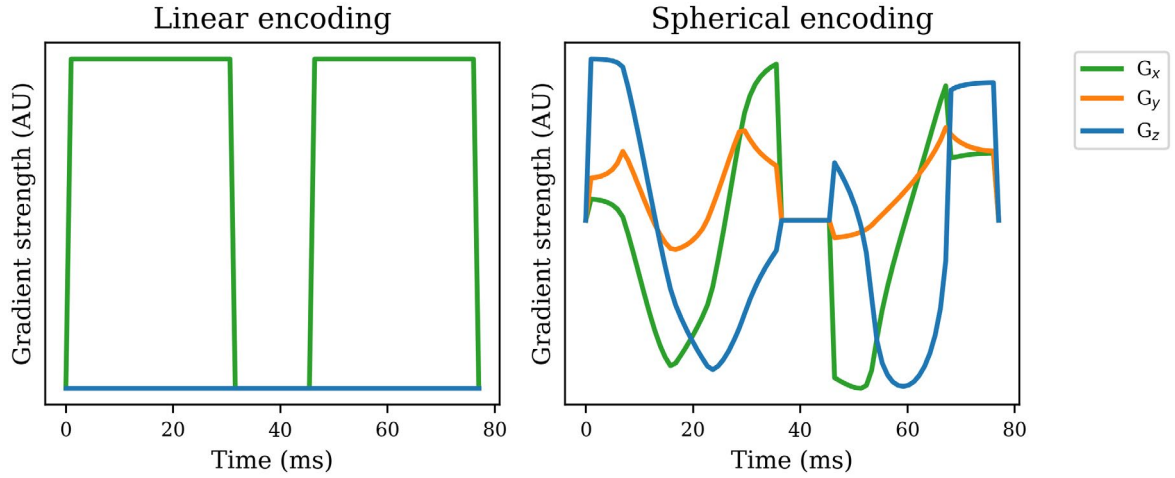

FIGURE 1 Optimized gradient waveforms encoding linear and spherical *b*-tensors. A 180° refocusing pulse was applied between the two parts of the waveform where gradient magnitude is zero

and

$$\mathbf{S} = \left(\ln S_1, \ldots, \ln S_n\right)^T \quad (4)$$

where S_i is the signal in the ith acquisition; n is the number of acquisitions; tensors are represented as column vectors in Voigt notation as described by Westin et al[11]; and the diagonal matrix $\mathbf{H}$ with elements $\mathbf{H}_{ii} = S_i$ was used to correct for heteroscedasticity in the log-transformed data. The matrix inversion in Equation 2 was performed using the Moore-Penrose pseudoinversion in Numpy.[44]

The MD and FA were calculated from the estimated diffusion tensor eigenvalues. The value of μFA and measure of normalized size variance (C_{MD}) were calculated from the estimated covariance tensor elements according to

$$\mu FA = \sqrt{\frac{3}{2}\frac{(\mathbb{C} + \mathbf{D}\otimes\mathbf{D}) : \mathbb{E}_{shear}}{(\mathbb{C} + \mathbf{D}\otimes\mathbf{D}) : \mathbb{E}_{iso}}} \quad (5)$$

and

$$C_{MD} = \sqrt{\frac{C : \mathbb{E}_{bulk}}{(\mathbb{C} + \mathbf{D}\otimes\mathbf{D}) : \mathbb{E}_{bulk}}}, \quad (6)$$

where $\mathbb{E}_{shear}$, $\mathbb{E}_{iso}$, and $\mathbb{E}_{bulk}$ were defined as specified by Westin et al.[11]

2.5 | Statistical analysis

Bland-Altman plot was used to assess the robustness of the subsampled data by doing a voxel-wise comparison of microstructural maps using the full data set and subsampled data set.

The reproducibility of the protocol was assessed using the coefficient of variation (CV): $CV(\%) = \mu/\sigma * 100$, where μ is the sample mean and σ is the within-subject SD that was estimated using one-way repeated-measures analysis of variance in Pingouin.[45]

3 | RESULTS

Figure 2 shows the hippocampal internal architecture in mean diffusion-weighted images of both *b*-tensor shapes over multiple slices. At 1.5-mm isotropic resolution, contrast within the hippocampus allows visualization of hippocampal digitations (arrow), white-matter structures known as stratum lacunosum moleculare (SLM; arrowheads), and its exterior outline.

Figure 3 shows the powder-averaged signal (ie, signal averaged over all gradient directions) for both *b*-tensor shapes and their difference. The divergence between the powder-averaged signals with an increasing *b*-value, the hallmark effect of microscopic anisotropy, was observed in the hippocampus. Additionally, the powder-averaged signal acquired with spherical tensors did not follow a mono-exponential decay (Figure 3B), indicating isotropic size variance.

The FA, MD, μFA, and C_{MD} maps in one of the volunteers are shown in Figure 4A-D alongside the histograms of the values of the microstructural metrics across all 8 volunteers over the whole hippocampal voxel, left and right sides combined. Averaged across the hippocampus volumes of all volunteers, MD was 1.06 ± 0.37 $\mu m^2/ms$, FA was 0.20 ± 0.09, μFA was 0.47 ± 0.13, and C_{MD} was 0.17 ± 0.05, where the reported numbers correspond to the mean and SD, respectively. The magnitude of μFA was significantly higher than FA (two-tailed paired t-test, $p < .05$), indicating an orientation dispersion in the microscopic diffusion environments in the hippocampus.

The subsampled data set for FA, MD, μFA, and C_{MD} maps in one of the volunteers is shown in Figure 4E-H alongside a Bland-Altman plot showing the differences between the metrics extracted from the full data set against their mean value across all volunteers' hippocampal volume. The mean difference was 0.02 for MD, 0.12 for FA, 0.04 for μFA, and 0.01 for C_{MD}, suggesting that the minimal protocol can be reliably applied in quantifying mean DTI and QTI metrics over the hippocampus in situations with time constraints. Because the differences are not normally distributed, the 95% central range of the differences was used to assess the limits of agreement, which were [−0.21, 0.29] for MD, [−0.34, 0.06] for FA, [−0.22, 0.10] for μFA, and [−0.08, 0.10] for C_{MD}.

The microstructural metrics from scan–rescan experiments are reported, and overlap of the histograms are plotted in Figure 5. For each volunteer (volunteer 1: blue/green, volunteer 2: olive/pink), Figure 5A shows the overlap of microstructural metrics derived from the full protocol and Figure 5B shows overlap of microstructural metrics derived from the subsampled protocol. To quantify the reproducibility of the parameter estimates, CV was calculated to compare the means of the distributions of the microstructural metrics in the hippocampus (Supporting Information Table S2). The low CV values show small fluctuations and suggest that the protocol can be used to measure subject-specific information reproducibly. In the reproducibility analysis of both data, the CV of FA (full data: 4%, subsampled data: 11.5%) was higher than that of μFA (full data: 1%, subsampled data: 5%) because its value

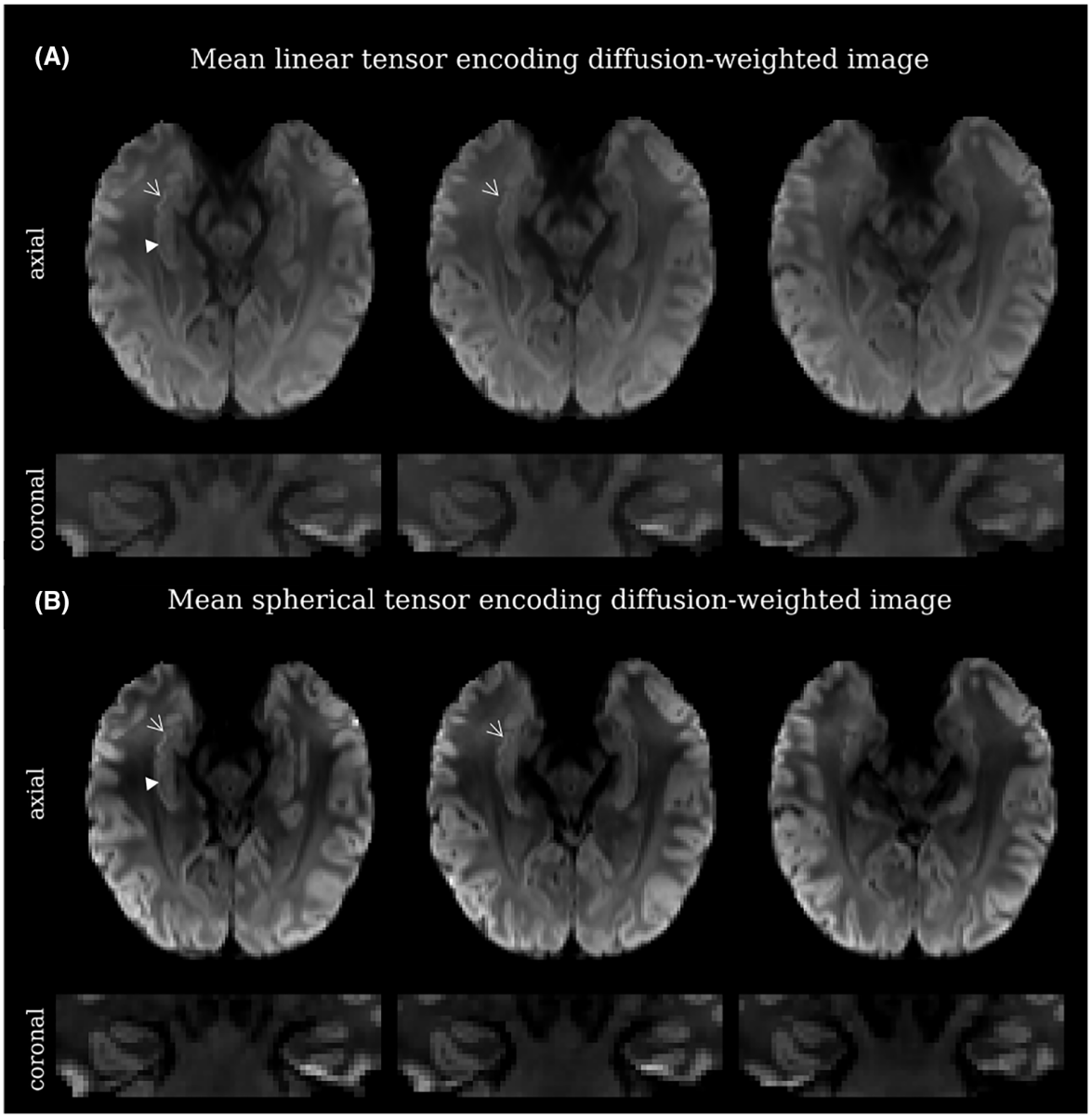

FIGURE 2 Three sequential axial and coronal sections of mean diffusion-weighted images at 1.5-mm isotropic resolution from one representative acquired with linear *b*-tensors (A) and spherical *b*-tensors (B). Hippocampal internal anatomy, such as the head digitations (arrow) and the darker lines of stratum lacunosum moleculare (SLM; arrowheads), can be visualized

was lower. The results suggest that the reproducibility of the QTI metrics is comparable to the DTI metrics.

4 | DISCUSSION

This study demonstrates the capacity of yielding high-resolution (1.5-mm isotropic) diffusion images of the human hippocampus at 3 T, allowing visualization of hippocampal details such as digitations in the head as well as SLM, and provides evidence that MDE methods are capable of probing microscopic anisotropy in the human hippocampus in vivo.

The clinical value of microstructural imaging of the hippocampus has been shown in previous studies.[25,46–48] For example, decreased FA and elevated MD values were observed in the ipsilateral hippocampus of temporal lobe epilepsy patients with mesial temporal sclerosis.[49,50] Although FA is a sensitive parameter, it has a disadvantage in that it lacks specificity and sensitivity. Our protocol leverages the most recent advances in MDE and is able to provide a more detailed characterization of the hippocampal microstructure. The hallmark effect of microscopic anisotropy (increasing divergence between LTE and STE with increasing *b*-value) is demonstrated throughout the hippocampus across all volunteers (Figure 3). Mean μFA

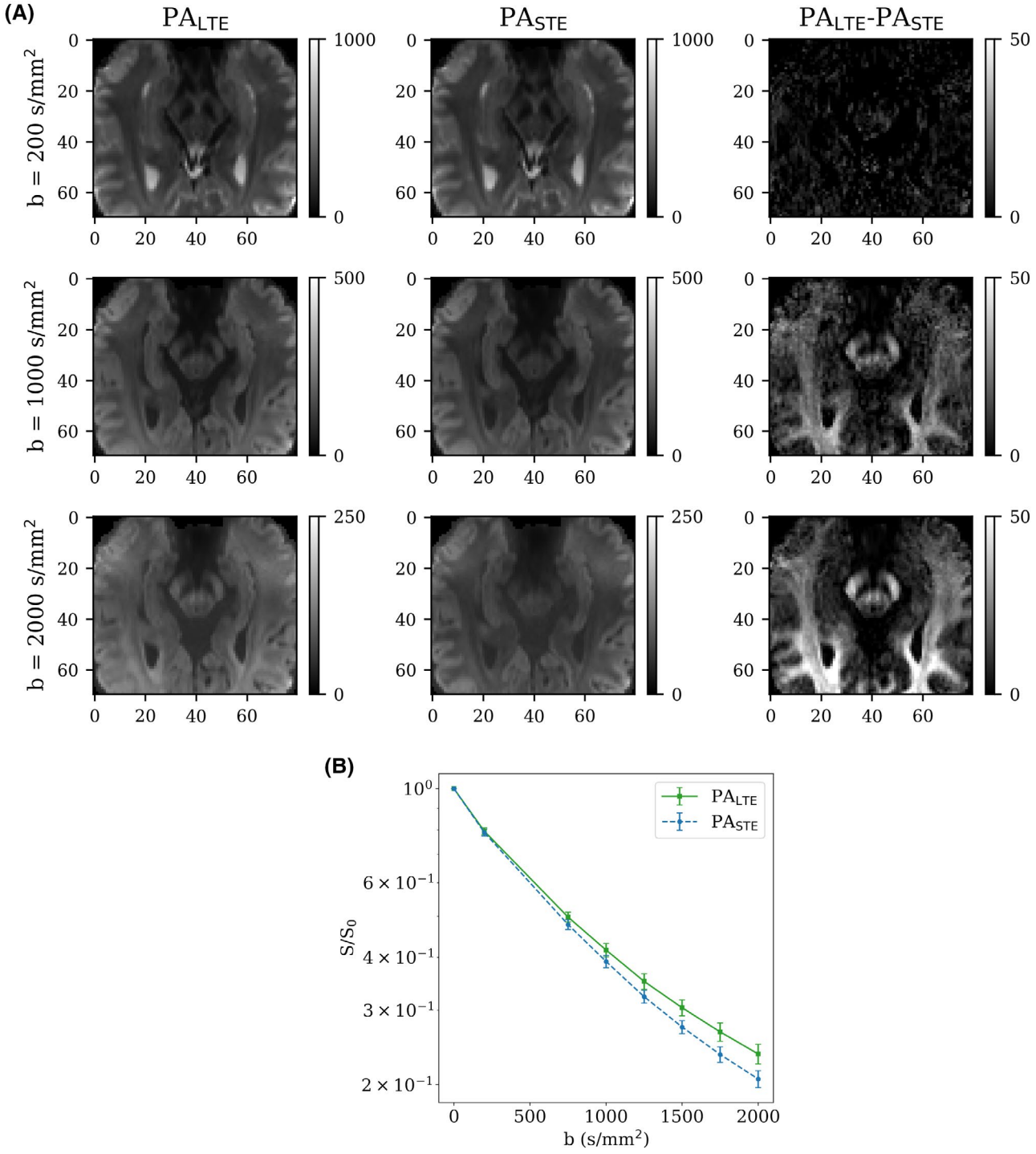

FIGURE 3 (A) Powder-averaged data acquired with linear *b*-tensors (PA_{LTE}), spherical *b*-tensors (PA_{STE}), and the difference between the two (PA_{LTE}-PA_{STE}), shown in one of the volunteers for three *b*-values. B, Powder-averaged signal decay averaged over the hippocampus volume of 8 volunteers. The difference between the powder-averaged signals acquired with the two tensor shapes increases with the *b*-value in voxels with microscopic diffusion anisotropy

was greater than mean FA across all volunteers, indicating that there is anisotropy present in the hippocampus that is masked by the low FA. For instance, as part of the trisynaptic circuit, it is known that the granule cells of the dentate gyrus project through their mossy fibers to the CA3 substructure of the hippocampus, and orthogonally cross the apical dendrites of CA3 pyramidal neurons.[51] Although these fiber architectures demonstrate coherence, DTI underestimates the FA of non-monopolar coherences due its confoundment.[52] Because μFA may provide a more accurate assessment of microstructural integrity compared with conventional FA, one can hypothesize that μFA may

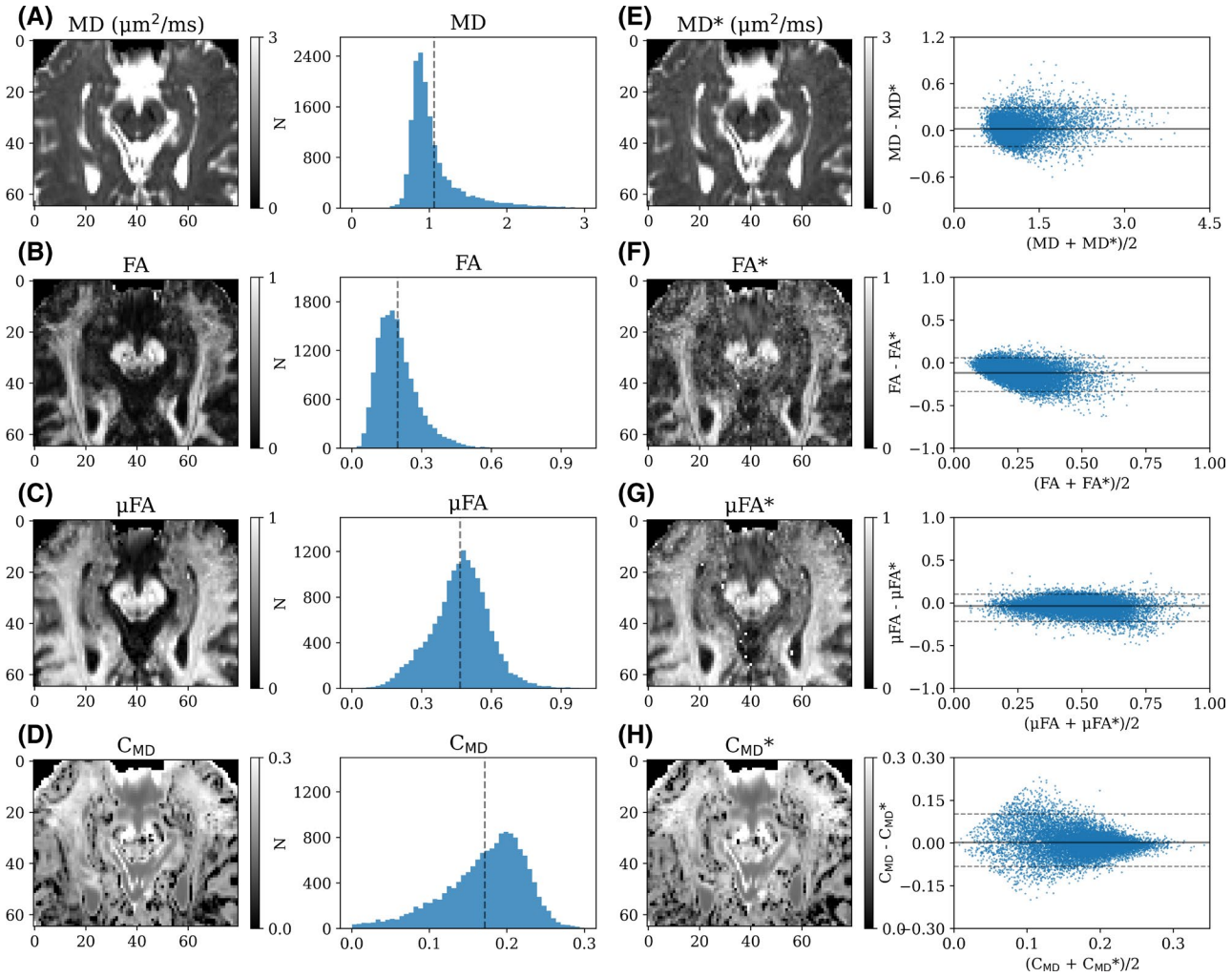

FIGURE 4 (A–D) Microstructural maps for a single, selected volunteer and next to it, distributions of their values in the hippocampus across all 8 volunteers. The dashed lines in the histograms depict the mean value. Top to bottom: A mean diffusivity (MD) (A), fractional anisotropy (FA) (B), microscopic fractional anisotropy (μFA) (C), and normalized size variance (C_{MD}) (D). E-H, Microstructural maps calculated from the subsampled data set in one of the volunteers. Next to it, a voxel-wise comparison between the maps calculated using the full data set and the subsampled data set (*) across all volunteers. The solid line represents the mean difference, and the dashed lines represent the 2.5th and 97.5th percentiles of the distribution of the differences. Top to bottom: Subsampled MD* (E), FA* (F), μFA* (G), and C_{MD}* (H)

help elucidate pathophysiological mechanisms that typically occur in the hippocampus such as abnormalities in mossy fibers and the granule cell layer in epilepsy.[53] Although this hypothesis will require future clinical studies, the current study focused on establishing a protocol with an in-house-developed sequence, and obtaining μFA measures in healthy volunteers serves as baseline data and proof of principle.

A shorter acquisition that is feasible in a clinical setting by subsampling the full data was also defined. The full acquisition had a scan time of 1 hour, whereas the subsampled data could be acquired in just 14 minutes. The subsampled data had slightly higher mean and variance, but it yielded similar maps to the full data with small mean differences (Figure 4E-H). The subsampled protocol could therefore be feasibly added on to an existing protocol for measure of novel microstructural information in clinical studies.

Two subjects were rescanned 7 weeks later from their initial scan, to test the reproducibility of the protocol. The CV was estimated for the full protocol of scan and rescan diffusion parameters, regardless of the subject, and the low CV values demonstrated the reproducibility of the model fitting (Supporting Information Table S2). In the subsampled protocol, microstructural metrics histogram overlap is slightly broader compared with the full protocol (Figure 5A,B). Volunteer 1's subsampled FA (Figure 5B) in particular shows a broader overlap, which addresses a limitation in the current subsampling method. The subsampling technique here is not

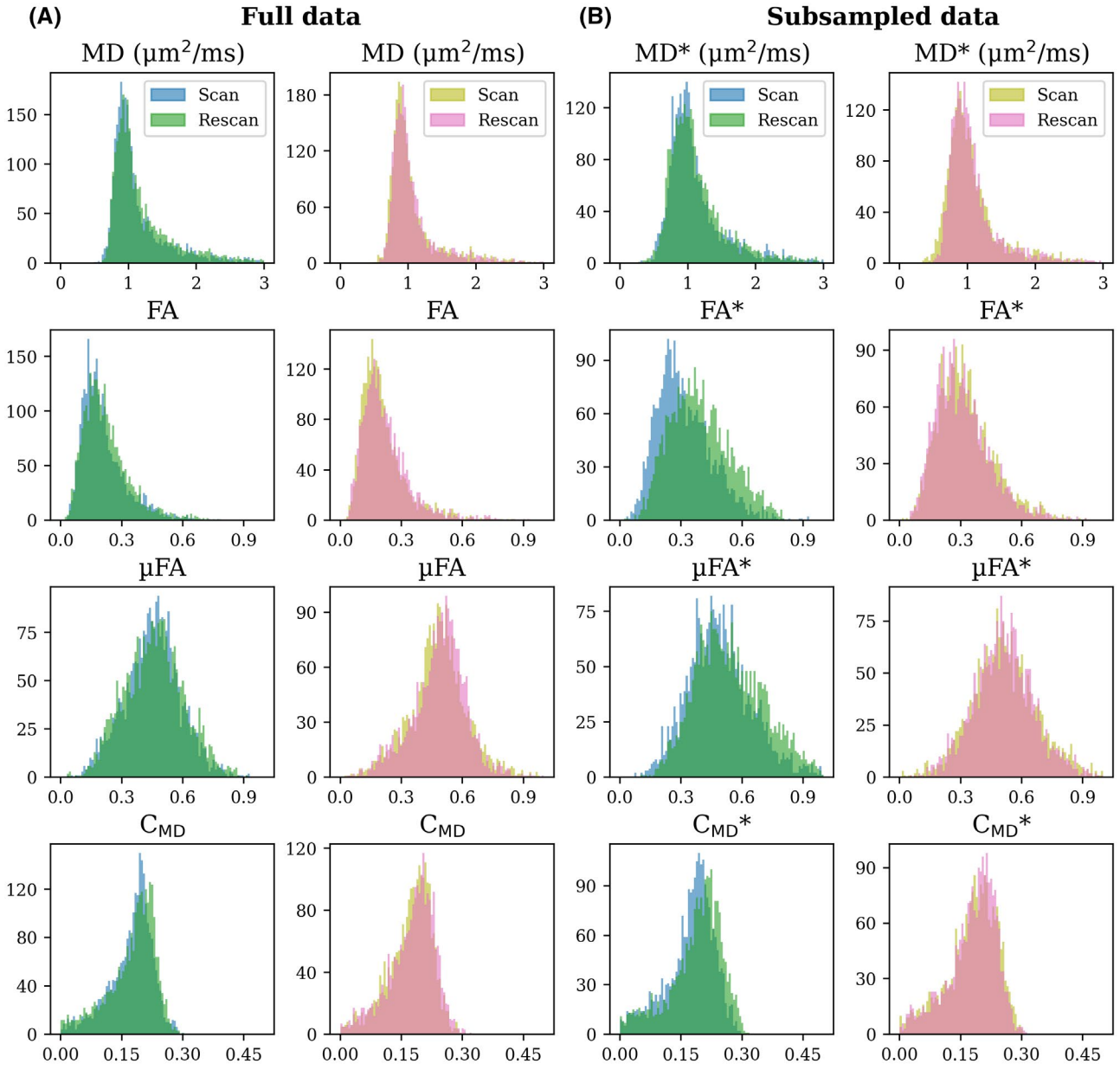

FIGURE 5 Assessment of scan–rescan reproducibility in subject 1 (in blue/green) and subject 2 (in olive/pink) for full q-space trajectory imaging (QTI) protocol (1 hour) (A) and for subsampled protocol (14 minutes) (B) reporting MD, FA, μFA, and C_{MD}

optimized but rather a pragmatic choice with added constraints. The first constraint was to have a protocol under 15 minutes, as this is what we consider to be an acceptable imaging time in the clinical setting. Second was to have more directions at the higher shells for model fitting purposes, as the hallmark effect of μFA is diverging signal between LTE and STE, which increases with increasing *b*-value.[18] Following these principles, subsampled directions were chosen to be uniformly distributed around the surface of half a sphere (see also Supporting Information Table S1). Therefore, the subsampled protocol is suboptimal in that it is intended for fitting μFA and estimates noisier maps for FA. This limitation will be addressed in the future for an optimized subsampled protocol that accurately estimates both QTI and DTI metrics.

Other limitations should be addressed in future research. In terms of acquisition, the current protocol suffers from a long TE. This can be reduced by implementing planar tensor encoding (PTE) instead of STE.[54] "Planar" *b*-tensors are shaped like discs. Planar tensor encoding allows more efficient experimental designs and waveforms. The current sequence interleaved LTE and STE so that it was less straining on the gradient amplifiers of the scanner, but with PTE, more efficient interleaving could be achieved, such as high *b*-value PTE followed by low *b*-value LTE. Planar tensor encoding would allow reduction of the current TE, which will

overall help to further reduce scan time. Furthermore, one could yield a faster, optimized protocol by reducing the directions used with STE, as they are redundant and only increasing SNR.[55,56] This could also enable an increase in spatial resolution, allowing investigation of hippocampal substructures. However, one must be cautious when using automated segmentation methods for hippocampal subfield selection, as even with 1-mm isotropic resolution, substructures can be difficult to visualize.[57] Future work will involve ways to manually segment the hippocampal subregions to derive QTI metrics, as examination of more specific microstructural parameters may give a better indication of hippocampal connectivity and how abnormalities such as hippocampal sclerosis can be better characterized using MDE sequences.

Overall, this work shows the feasibility of high-resolution microscopic anisotropy imaging in the healthy hippocampus. This provides microstructural information that cannot be acquired by conventional diffusion encoding.

5 | CONCLUSION

In this study, a multidimensional diffusion imaging protocol was developed and applied to image the healthy human hippocampus with high resolution at 3 T. q-Space trajectory imaging was used to estimate microscopic diffusion anisotropy, and isotropic size variance in the hippocampus and reference values were reported.

ACKNOWLEDGMENT

The authors thank Enrico Kaden for the development of the bespoke diffusion EPI sequence, and Tina Banks at Great Ormond Street Hospital for her invaluable help with the scans.

ORCID

Jiyoon Yoo https://orcid.org/0000-0003-2802-6256

REFERENCES

1. Assaf Y, Johansen-Berg H, Thiebaut de Schotten M. The role of diffusion MRI in neuroscience. *NMR Biomed*. 2019;32:1-16.
2. Behrens TEJ, Johansen-Berg H. *Diffusion MRI: From Quantitative Measurement to in-Vivo Neuroanatomy*. Academic Press; 2009.
3. Basser PJ, Mattiello J, LeBihan D. MR diffusion tensor spectroscopy and imaging. *Biophys J*. 1994;66:259-267.
4. Basser PJ, Pierpaoli C. Microstructural and physiological features of tissues elucidated by quantitative-diffusion-tensor MRI. *J Magn Reson*. 2011;213:560-570.
5. Jensen JH, Helpern JA, Ramani A, Lu H, Kaczynski K. Diffusional kurtosis imaging: the quantification of non-Gaussian water diffusion by means of magnetic resonance imaging. *Magn Reson Med*. 2005;53:1432-1440.
6. Novikov DS, Fieremans E, Jespersen SN, Kiselev VG. Quantifying brain microstructure with diffusion MRI: theory and parameter estimation. *NMR Biomed*. 2018;1-53.
7. Tournier JD, Calamante F, Connelly A. Robust determination of the fibre orientation distribution in diffusion MRI: non-negativity constrained super-resolved spherical deconvolution. *NeuroImage*. 2007;35:1459-1472.
8. Shemesh N, Jespersen SN, Alexander DC, et al. Conventions and nomenclature for double diffusion encoding NMR and MRI. *Magn Reson Med*. 2016;75:82-87.
9. Stejskal EO, Tanner JE. Spin diffusion measurements: spin echoes in the presence of a time-dependent field gradient. *J Chem Phys*. 1965;42:288-292.
10. Szczepankiewicz F, Lasič S, van Westen D, et al. Quantification of microscopic diffusion anisotropy disentangles effects of orientation dispersion from microstructure: applications in healthy volunteers and in brain tumors. *NeuroImage*. 2015;104:241-252.
11. Westin C-F, Knutsson H, Pasternak O, et al. Q-space trajectory imaging for multidimensional diffusion MRI of the human brain. *NeuroImage*. 2016;135:345-362.
12. Cory D, Garroway A, Miller J. Applications of spin transport as a probe of local geometry. In: *Abstracts of Papers of the American Chemical Society*. Vol 199. Washington, DC: American Chemical Society; 1990:105-POLY.
13. Eriksson S, Lasic S, Topgaard D. Isotropic diffusion weighting in PGSE NMR by magic-angle spinning of the q-vector. *J Magn Reson*. 2013;226:13-18.
14. Topgaard D. Multidimensional diffusion MRI. *J Magn Reson*. 2017;275:98-113.
15. Jespersen SN, Lundell H, Sønderby CK, Dyrby TB. Orientationally invariant metrics of apparent compartment eccentricity from double pulsed field gradient diffusion experiments. *NMR Biomed*. 2013;26:1647-1662.
16. Kamiya K, Kamagata K, Ogaki K, et al. Brain white-matter degeneration due to aging and Parkinson disease as revealed by double diffusion encoding. *Front Neurosci*. 2020;14:1-15.
17. Chen C, Li H, Ding F, Yang L, Huang P, Wang S. Alterations in the hippocampal-thalamic pathway underlying secondarily generalized tonic-clonic seizures in mesial temporal lobe epilepsy: a diffusion tensor imaging study. *Epilepsia*. 2019;60:121-130.
18. Lasič S, Szczepankiewicz F, Eriksson S, Nilsson M, Topgaard D. Microanisotropy imaging: quantification of microscopic diffusion anisotropy and orientational order parameter by diffusion MRI with magic-angle spinning of the q-vector. *Front Phys*. 2014;2:1-14.
19. Kerkelä L, Nery F, Callaghan R, et al. Comparative analysis of signal models for microscopic fractional anisotropy estimation using q-space trajectory encoding. *NeuroImage*. 2021;242:118445.
20. Scoville WB, Milner B. Loss of recent memory after bilateral hippocampal lesions. *J Neurol Neurosurg Psychiatry*. 1957;20:11-21.
21. Olton DS, Becker JT, Olton HGE, et al. Hippocampus, space, and memory. *Behav Brain Sci*. 1979;2:313-365.
22. Burgess N, Maguire EA, O'Keefe J. The human hippocampus and spatial and episodic memory. *Neuron*. 2002;35:625-641.
23. Maguire EA, Gadian DG, Johnsrude IS, et al. Navigation-related structural change in the hippocampi of taxi drivers. *Proc Natl Acad Sci USA*. 2000;97:4398-4403.

24. Shepherd TM, Özarslan E, Yachnis AT, King MA, Blackband SJ. Diffusion tensor microscopy indicates the cytoarchitectural basis for diffusion anisotropy in the human hippocampus. *Am J Neuroradiol*. 2007;28:958-964.
25. Nazem-Zadeh M-R, Schwalb JM, Elisevich KV, et al. Lateralization of temporal lobe epilepsy using a novel uncertainty analysis of MR diffusion in hippocampus, cingulum, and fornix, and hippocampal volume and FLAIR intensity. *J Neurol Sci*. 2014;342:152-161.
26. Alizadeh M, Kozlowski L, Muller J, et al. Hemispheric regional based analysis of diffusion tensor imaging and diffusion tensor tractography in patients with temporal lobe epilepsy and correlation with patient outcomes. *Sci Rep*. 2019;9:1-8.
27. Cherubini A, Péran P, Caltagirone C, Sabatini U, Spalletta G. Aging of subcortical nuclei: microstructural, mineralization and atrophy modifications measured in vivo using MRI. *NeuroImage*. 2009;48:29-36.
28. Yassa MA, Mattfeld AT, Stark SM, Stark CEL. Age-related memory deficits linked to circuit-specific disruptions in the hippocampus. *Proc Natl Acad Sci*. 2011;108:8873-8878.
29. Chiapponi C, Piras F, Fagioli S, Girardi P, Caltagirone C, Spalletta G. Hippocampus age-related microstructural changes in schizophrenia: a case-control mean diffusivity study. *Schizophr Res*. 2014;157:214-217.
30. Nazeri A, Mulsant BH, Rajji TK, et al. Gray matter neuritic microstructure deficits in schizophrenia and bipolar disorder. *Biol Psychiatry*. 2017;82:726-736.
31. Zhang Y, Schuff N, Jahng G-H, et al. Diffusion tensor imaging of cingulum fibers in mild cognitive impairment and Alzheimer disease. *Neurology*. 2007;68:13-19.
32. Fellgiebel A, Yakushev I. Diffusion tensor imaging of the hippocampus in MCI and early Alzheimer's disease. *J Alzheimer's Dis*. 2011;26:257-262.
33. Pereira JB, Valls-Pedret C, Ros E, et al. Regional vulnerability of hippocampal subfields to aging measured by structural and diffusion MRI. *Hippocampus*. 2014;24:403-414.
34. Köbe T, Witte AV, Schnelle A, et al. Vitamin B-12 concentration, memory performance, and hippocampal structure in patients with mild cognitive impairment. *Am J Clin Nutr*. 2016;103:1045-1054.
35. Treit S, Steve T, Gross DW, Beaulieu C. High resolution in-vivo diffusion imaging of the human hippocampus. *NeuroImage*. 2018;182:479-487.
36. Sjölund J, Szczepankiewicz F, Nilsson M, Topgaard D, Westin C-F, Knutsson H. Constrained optimization of gradient waveforms for generalized diffusion encoding. *J Magn Reson*. 2015;261:157-168.
37. Szczepankiewicz F, Westin CF, Nilsson M. Maxwell-compensated design of asymmetric gradient waveforms for tensor-valued diffusion encoding. *Magn Reson Med*. 2019;82:1424-1437.
38. Veraart J, Novikov DS, Christiaens D, Ades-aron B, Sijbers J, Fieremans E. Neuroimage denoising of diffusion MRI using random matrix theory. *NeuroImage*. 2016;142:394-406.
39. Kellner E, Dhital B, Kiselev VG, Reisert M. Gibbs-ringing artifact removal based on local subvoxel-shifts. *Magn Reson Med*. 2016;76:1574-1581.
40. Smith SM, Jenkinson M, Woolrich MW, et al. Advances in functional and structural MR image analysis and implementation as FSL. *NeuroImage*. 2004;23:S208-S219.
41. Manjón JV, Volbrain CP. An online MRI brain volumetry system. *Front Neuroinform*. 2016;10:1-14.
42. Romero J, Coupé P, Manjón JV, et al. HIPS: a new hippocampus subfield segmentation method. *NeuroImage* 2017;163:286-295.
43. Modat M, Ridgway GR, Taylor ZA, et al. Fast free-form deformation using graphics processing units. *Comput Methods Programs Biomed*. 2010;98:278-284.
44. van der Walt S, Colbert SC, Varoquaux G. The NumPy array: a structure for efficient numerical computation. *Comput Sci Eng*. 2011;13:22-30.
45. Vallat R. Pingouin: statistics in Python. *J Open Source Softw*. 2018;3:1026.
46. Bartsch T, Döhring J, Reuter S, et al. Selective neuronal vulnerability of human hippocampal CA1 neurons: lesion evolution, temporal course, and pattern of hippocampal damage in diffusion-weighted MR imaging. *J Cereb Blood Flow Metab*. 2015;35:1836-1845.
47. Hong YJ, Yoon B, Lim S-C, et al. Microstructural changes in the hippocampus and posterior cingulate in mild cognitive impairment and Alzheimer's disease: a diffusion tensor imaging study. *Neurol Sci*. 2013;34:1215-1221.
48. Tang X, Qin Y, Wu J, Zhang M, Zhu W, Miller MI. Shape and diffusion tensor imaging based integrative analysis of the hippocampus and the amygdala in Alzheimer's disease. *Magn Reson Imaging*. 2016;34:1087-1099.
49. Assaf BA, Mohamed FB, Abou-Khaled KJ, et al. Diffusion tensor imaging of the hippocampal formation in temporal lobe epilepsy. *Am J Neuroradiol*. 2003;24:1857-1862.
50. Salmenpera TM, Simister RJ, Bartlett P, et al. High-resolution diffusion tensor imaging of the hippocampus in temporal lobe epilepsy. *Epilepsy Res*. 2006;71:102-106.
51. Amaral DG, Witter MP. The three-dimensional organization of the hippocampal formation: a review of anatomical data. *Neuroscience*. 1989;31:571-591.
52. Shepherd TM, Özarslan E, King MA, Mareci TH, Blackband SJ. Structural insights from high-resolution diffusion tensor imaging and tractography of the isolated rat hippocampus. *NeuroImage*. 2006;32:1499-1509.
53. Coras R, Milesi G, Zucca I, et al. 7T MRI features in control human hippocampus and hippocampal sclerosis: an ex vivo study with histologic correlations. *Epilepsia*. 2014;55:2003-2016.
54. Szczepankiewicz F, Hoge S, Westin CF. Linear, planar and spherical tensor-valued diffusion MRI data by free waveform encoding in healthy brain, water, oil and liquid crystals. *Data Br*. 2019;25:104208.
55. Nilsson M, Szczepankiewicz F, Brabec J, et al. Tensor-valued diffusion MRI in under 3 minutes: an initial survey of microscopic anisotropy and tissue heterogeneity in intracranial tumors. *Magn Reson Med*. 2020;83:608-620.
56. Szczepankiewicz F, Sjölund J, Ståhlberg F, Lätt J, Nilsson M. Tensor-valued diffusion encoding for diffusional variance decomposition (DIVIDE): technical feasibility in clinical MRI systems. Chen X, ed. *PLoS One*. 2019;14:e0214238.
57. Wisse LEM, Chételat G, Daugherty AM, et al. Hippocampal subfield volumetry from structural isotropic 1 mm3 MRI scans: a note of caution. *Hum Brain Mapp*. 2021;42:539-550.

SUPPORTING INFORMATION

Additional supporting information may be found in the online version of the article at the publisher's website.

TABLE S1 The diffusion sequence consisting of interleaved LTE and STE waveforms for full dataset (1 hour) and subsampled dataset (14 minutes)

TABLE S2 Scan-rescan microstructural metrics derived from full dataset and the subsampled dataset (*) across volunteer 1 and 2 showing mean, standard deviation (SD) and coefficient of variation (CV)

How to cite this article: Yoo J, Kerkelä L, Hales PW, Seunarine KK, Clark CA. High-resolution microscopic diffusion anisotropy imaging in the human hippocampus at 3T. *Magn Reson Med*. 2021;00:1–11. doi:10.1002/mrm.29104